



Characterization of the as-cast microstructure and selected properties of the X-40 Co-based superalloy produced via lost-wax casting

Łukasz Rakoczy¹ · Małgorzata Grudzień-Rakoczy² · Rafał Cygan³ · Bogdan Rutkowski¹ · Tomasz Kargul¹ · Tomasz Dudziak² · Ewa Rząd² · Ondrej Milkovic^{4,5} · Anna Zielińska-Lipiec¹

Received: 5 February 2022 / Revised: 22 April 2022 / Accepted: 4 May 2022 / Published online: 9 June 2022
© Wrocław University of Science and Technology 2022, corrected publication 2022

Abstract

The X-40 Co-based superalloy is often used in the aerospace industry directly in as-cast condition and its analysis in this state is essential to understand further possible phase transformations during service. With this in mind, this work focuses on characterizing the material's as-cast microstructure, phase transformation temperatures and oxidation resistance. Observations and analyses were performed via thermodynamic simulations, X-ray diffraction (XRD), light microscopy (LM), scanning electron microscopy (SEM), scanning-transmission electron microscopy (STEM-HAADF), energy-dispersive X-ray spectroscopy (EDX), dilatometry (DIL) and differential scanning calorimetry (DSC). The microstructure of the dendritic regions consisted of the α matrix, with MC, M_7C_3 and $M_{23}C_6$ carbides being present in the interdendritic spaces. Based on DIL, it was found that precipitation of the Cr-rich carbides from the saturated α matrix may occur in the range 650–750 °C. DSC determined the incipient melting and liquidus temperatures of the X-40 superalloy during heating to be 1405 °C and 1421 °C, respectively. Based on oxidation resistance tests carried out at 860 °C, it was found that the mass gain after 500 h exposure was 3 times higher in the air than in steam.

Keywords Cobalt superalloy · Jet engine · Investment casting · M_7C_3 · Oxidation

1 Introduction

The main advantages of Co-based superalloys over Ni- or Fe-based ones are their higher melting point [1], flatter stress rupture curves [2], increased hot-corrosion resistance in service atmospheres [3], low susceptibility to cracking during welding and good thermal fatigue resistance [4].

Cobalt-based alloys have been used to manufacture various components, such as vanes or combustion chambers in gas turbines (both industrial-type and aero-engines). The alloys can be implemented as wrought [5] or as precision-cast parts [6]. The importance of Co greatly increased during the development and manufacturing of the turbosupercharger, early in World War II. The Co-based alloy, widely known as Vitallium was found to have a strength and microstructural stability that made it suitable for bucket operating conditions (> 500 °C). Not long after that, a modified Vitallium marked as HS-21 was designed for manufacturing high-temperature components. With the material successfully meeting the application requirements under industrial conditions, its use was further extended to buckets and guide vanes for aircraft turbojet engines that operated at very high temperatures (for those time) up to 815 °C. Since then, the intensive work over developing alloys resulted in the group of materials we know today, i.e. superalloys. Active alloy-development programs have led to the production of a variety of important Co-based superalloys, like X-40 or its other grades, X-45 and FSX-414 [7]. The experience acquired during the industrial implementation of these superalloys makes them highly reliable

✉ Łukasz Rakoczy
lrakoczy@agh.edu.pl

¹ Faculty of Metals Engineering and Industrial Computer Science, AGH University of Science and Technology, Mickiewicza 30, 30-059 Kraków, Poland

² Łukasiewicz Research Network-Kraków Institute of Technology, Zakopiańska 73, 30-418 Kraków, Poland

³ Investment Casting Division, Consolidated Precision Products Corporation, Hetmańska 120, 35-078 Rzeszów, Poland

⁴ Institute of Materials Research, Slovak Academy of Sciences, Watsonova 47, 040 01 Kosice, Slovakia

⁵ Institute of Experimental Physics, Slovak Academy of Sciences, Watsonova 47, 040 01 Kosice, Slovakia

and more difficult to replace by other materials. Moreover, Co-based alloys have gained a prominent position due to the possibility for most of them to be melted in air and remelted under air or argon, as well as their good castability [8] and repairability [9]. Cobalt has two allotropes, where the hexagonal-close-packed (HCP) crystal structure is stable up to 417 °C, whereas above this temperature the face-centered-cubic crystal structure (α) appears [10]. Alloying elements like Ni, C and Fe tend to stabilize the FCC structure, while Mo and W stabilize the HCP structure [11, 12]. Chromium is the main alloying element increasing oxidation and hot corrosion resistance, additionally forming M_7C_3 , $M_{23}C_6$ and M_3C_2 carbides. The Mo and W are responsible for solid-solution strengthening and can create MC and M_6C carbides [13]. Co-based superalloys usually contain between 0.4 and 1.0% wt. carbon [14], which is a relatively high value compared to Ni-based superalloys [15]. The carbides' networks formed during casting solidification are relatively stable and relevant for high-temperature strength [16]. Hot-working leading to a change in carbide networks can increase the tensile strength at intermediate temperatures [17], however, at the expense of creep resistance at elevated temperatures (e.g. MAR-M 509) [18]. Geometrically close-packed phases, like Ni_3Al , can also be present in the microstructure, however, their instability at high temperatures hinders them from achieving high commercial status [19].

Several studies have been carried out on the X-40 alloy [20–22]. Kamma et al. [20] carried out tests of the fatigue resistance of the Ni-based superalloy 718 micro-spark coated with X-40, as a material characterized by increased wear and oxidation resistance. The authors stated, based on the fatigue experiments performed at 480 °C and 650 °C, that the fatigue life of Alloy 718 with an X-40 layer was comparable or slightly improved compared to the uncoated Ni-based superalloy. No spalling of the X-40 coating was observed during the performed fatigue experiments. The authors suggested that the load transfer capability may play a significant role, what with the X-40 layer's increased elastic modulus during the high-temperature exposure and the presence of compressive stresses at Alloy 718's surface. The elastic modulus of the as-deposited X-40 layer was equal to 40 GPa, almost 5 times smaller than that of the Alloy 718 substrate, however, when exposed to 650 °C this value increased approx. 2.5 times. Schoonbaert et al. [21] proposed a new braze repair scheme, in which Ni-based alloys repair the X-40 substrate in both narrow and wide gap configurations. Based on the microstructure analysis, the authors stated that the Ni-base braze alloy BNi-9 (also known as Ni-276 and Amdry 775) can be used to repair the as-cast Co-based X-40 superalloy without the formation of detrimental phases in the braze and especially interface X-40/braze regions. They concluded that the high carbon concentration in the X-40 superalloy may have played a significant role in preventing the TCP phases

formation during brazing and subsequent long-term service at elevated temperatures. Ghasemi et al. [22] investigated the influence of partial solution treatment (1200 °C, 2 h) and the subsequent cooling procedure (cooling in air, with a furnace or in graphite powder) on the microstructure and mechanical properties of the X-40 superalloy. Based on the microstructure analysis, it was shown that regardless of the applied cooling rate, secondary carbides form during cooling, and the specimens are characterized by almost the same microstructure and mechanical properties, which eliminates the need for the aging treatment. The partial dissolution of the continuous network of M_7C_3 carbides was observed during partial solution treatment, with the transformation of M_7C_3 carbides to $M_{23}C_6$ and the formation of fine secondary $M_{23}C_6$ carbides during the cooling after heat treatment. Significant differences between the size and volume fraction of the secondary $M_{23}C_6$ carbides were not detected during the investigated cooling procedures. The heat treatment of the X-40 Co-based superalloy allows obtaining in all samples the time to rupture during creep test (815 °C/210 MPa) above 30 h.

The X-40 Co-based superalloy is often used in as-cast condition for industrial applications. Solution treatment to induce the complete dissolution of primary carbides with subsequent ageing to precipitate secondary carbides in the α matrix is not recommended. Therefore, it is important to obtain more information on the stability of the X-40 Co-based superalloy and its properties directly in the as-cast state. The main aim of this work was to investigate in detail the properties of the X-40 Co-based superalloy, including strengthening phases, their stability with increasing temperatures, and finally the alloy's oxidation resistance in two oxidizing atmospheres.

2 Experimental procedure

The X-40 Co-based superalloy was used as the experimental casting material and gating system. The whole investment casting process was performed in the Investment Casting Division of Consolidated Precision Products Corp. Rzeszow Poland, and all technological conditions were as similar as possible to internal standards accepted by aerospace customers. Wax pattern plates with dimensions 160×80×8 mm with a gating system were combined into a set. Four vents were developed to stabilize and strengthen the wax model and to facilitate correct dewaxing. The molds were produced through a “dip and stucco” method, where each layer was formed by dipping the wax pattern into a slurry (binder and filler) and then covering it in a coarse dry backup. After drying, the molds were dewaxed in a boiler clave to remove any residual wax, and finally were covered by alumina silicate Fiberfrax heat insulation. The pouring process of the X-40 superalloy was

carried out in a Retech double-chamber vacuum furnace. A ceramic mold was placed in the chamber of the furnace and preheated at 1240 °C for 120 min. The 4-kg ingot was inductively melted under vacuum (2.9×10^{-3} Pa). The liquid superalloy was poured into the mold at 1480 °C and subsequently displaced to the cooling zone of the furnace (in about 10 s). After solidification and cooling down to room temperature, the mold was knocked away, and the cast plates were cut off. The material's chemical composition determined by spark optical emission spectroscopy (OES) is presented in Table 1.

Thermodynamic simulations obtained using the ThermoCalc software (version 2021a, Stockholm, Sweden), were carried out to make a Scheil solidification simulation and calculate phase stability under equilibrium conditions in the range from 600 to 1400 °C. The as-cast superalloy was subjected to X-ray diffraction (XRD) to identify the phases. $20 \times 20 \times 8$ mm samples, with mechanically polished surface, were prepared. Measurements were made in Bragg–Brentano geometry using a Bruker D8 Advance diffractometer equipped with cobalt radiation ($\lambda = 1.789$ Å). Measurements were made at room temperature in the range of $2\theta = 30$ – 120° , with a step size of 0.04° .

The X-40 superalloy's microstructure studies included light microscopy (LM), scanning electron microscopy (SEM) and scanning-transmission electron microscopy-annular dark-field imaging (STEM-HAADF). The light microscopy studies were performed using a Leica DM1000 microscope on chemically etched (10 s) specimens, in a reagent consisting of 15 ml HNO_3 , 15 ml CH_3COOH , 60 ml HCL , 15 ml H_2O . The surface fraction of precipitates was estimated by the relative space taken up by a given microstructure constituent, which is the area fraction occupied by this constituent on the unit plane of the specimen. The images were binarized and subjected to a despeckle filter. The measurements were carried out based on 5 images captured at a magnification $50\times$. SEM observations were performed using a Phenom XL device, equipped with a backscattered electron (BSE) detector, and operated at an accelerating voltage of 20 kV. Energy-dispersive X-ray spectroscopy (SEM–EDX) measurements were performed to reveal the distribution of the alloying elements. Distribution maps and quantitative analyzes of selected areas were made (ZAF correction). The calculation of the partitioning coefficient of the alloying elements was carried out in accordance with the relationship $k^i = \frac{C_D^i}{C_0^i}$, where C_D^i —"i" element concentration in the dendrite core (point analysis), C_0^i —"i" element concentration in the area with dimensions 50×50 μm (area including dendritic cores and interdendritic spaces). STEM research was

carried out using the FEI Titan³ Cubed 2 60–300 high-resolution scanning-transmission electron microscope equipped with a ChemiSTEM chemical analysis system. Thin foils were prepared by grinding the material to a thickness of about 50 μm , cutting 3 mm discs, dimpling, and low-angle thinning with Ar^+ ions (PIPS of Gatan). Before loading into the microscope chamber, the specimens were plasma cleaned (NanoMill 1040 Fischione) to remove surface contaminations. The STEM imaging with high-angle annular-dark-field (HAADF) contrast and EDX mapping was used to characterize the structure. Phase identification was carried out using selected area electron diffraction (SAED), combined with EDX microanalysis. The electron diffraction patterns were interpreted using the JEMS software. The STEM-EDX data were acquired at 300 kV and then subjected to analysis using the Esprit software (Bruker, v1.9), in which the standardless Cliff-Lorimer quantification method was applied. Dilatometric tests were performed to analyze phase transformations as a function of temperature increase. Measurements were carried out using a RITA L78 dilatometer on cylindrical samples with a diameter of 3 mm and a length of 10 mm. The change in sample size was recorded from room temperature to 1280 °C at a heating rate of 0.08 °C/s. Differential scanning calorimetry (DSC) was carried out on a Netzsch STA 449F3 Jupiter equipped with a rhodium furnace, which can operate up to 1600 °C. It possesses a microbalance with a resolution of 10^{-6} g and is characterized by a calorimetric sensitivity of 0.1 mW. The aim of DSC was to determine phase transformation temperatures and the accompanying thermal effects during sample melting and solidification. In the high-temperature range, the transformation temperatures may be disturbed by the ongoing oxidation processes of the sample, significantly above the liquidus temperature of the alloy. Therefore, apart from the DSC signal for the activated thermal effects, changes in sample mass were additionally recorded. During the measurement, the samples' mass remained unchanged, proving the negligible oxidation processes of the analyzed superalloy and changes in its chemical composition. The mass of the analyzed samples was comparable and amounted to about 6 mg. Cylindrical samples were prepared, with a diameter of 4 mm and a length of about 1 mm. The device was calibrated by recording the melting temperatures and enthalpies of pure standard materials (In, Sn, Al, Au, Ni) and comparing the results obtained during the calibration with the nominal values of the standards. All the values recorded on the X-40 Co-based superalloy were corrected for the values resulting from the calibration of the device, which enabled the quantitative analysis of the thermal melting/solidification effects. The program included heating the sample in

Table 1 Chemical composition of the X-40 Co-based superalloy, wt%

Element	Cr	Ni	W	Si	C	Zr	Al	B	Fe	N	S	O	Co
Concentration	25.8	10.96	7.75	0.95	0.51	0.16	0.06	0.006	0.003	0.0019	0.0017	0.0003	Bal

an inert atmosphere from room temperature to 1465 °C (10 K/min), holding for 3 min and cooling (10 K/min). The tests were carried out in an argon atmosphere with a purity of 6 N. Prior to the measurements, the furnace was twice pumped and flushed with inert gas. In addition, a zirconium oxygen trap was placed in the chamber, to bind residual oxygen and prevent sample oxidation. Sample analyzes were performed in 85 μl Al_2O_3 crucibles with lids. Oxidation resistance experiments were carried out on heat-treated samples (cuboids with dimensions 20 \times 8 \times 5 mm). The samples were ultrasonically cleaned in isopropanol for 15 min at 40 °C. After drying, the samples were weighed using an analytical balance (accuracy 10⁻⁵ g). Next, the samples were exposed to air and steam separately. The steam oxidation rig is shown in Fig. 1 [23–25].

The steam is generated by pumping highly purified double deionized water (minimize oxygen potential) from a reservoir placed underneath the furnace. In the furnace water, steam passes over the tested samples and flows into a condenser before the water returns to the reservoir. The rig uses a stainless steel cylinder (316L SS) lined with ceramic lining to prevent the steam reacting with the inner part of the cylinder, where the rig inlets of nitrogen and water are connected. 2 h prior to the experiment, the interior of the rig was flushed with nitrogen and heated for the next 2 h at 150 °C. Afterwards, the rig was heated at a rate of 2.5 °C/min until reaching the required temperature and the nitrogen flow was closed. A peristaltic pump was operated at a flow rate of 2.833 ml/min to start the steam oxidation process. Finally, when the cycle was completed, the rig turned off

automatically via the Eurotherm controller and was left to cool. The peristaltic pump was turned off manually when the rig's temperature reached around 200–300 °C, to avoid steam condensation.

X-40 Co-based superalloy samples, similar to those used in the steam oxidation process, were exposed to air at 860 °C for 500 h. Similar to steam oxidation, air oxidation was interrupted after 125, 250, 375 and finally 500 h to measure the mass gain of the exposed material. The ramp rate was 2.5 °C/min until reaching the final temperature, after which the rig turned off automatically and cooled to room temperature together with the samples inside the silica tube. The rig was calibrated to find the furnace's hot zone, using thermocouple K. The samples were placed on a non-reactive Al_2O_3 holder and inserted into the rig's hot zone. Finally, the SiO_2 tube inserted into the tubular furnace was closed at both ends by ceramic plugs to prevent humid air entering from the ambient atmosphere. The air oxidation rig used in this work is presented in Fig. 2.

After the oxidation process, the phase composition of the formed oxide scales was analyzed via XRD using a Philips X'Pert Pro MPD diffractometer, with Cu $K\alpha$ radiation, in Bragg–Brentano geometry. Measurements were performed at room temperature in the range of $2\theta = 30\text{--}80^\circ$, with a scanning step size of 0.00836°. The morphology and chemical composition of the oxides (semi-quantitative measurements) were analyzed by SEM–EDX on the samples' surface and cross-sections. The set-up was the same as during the base material investigation.

Fig. 1 Steam oxidation rig used in the study

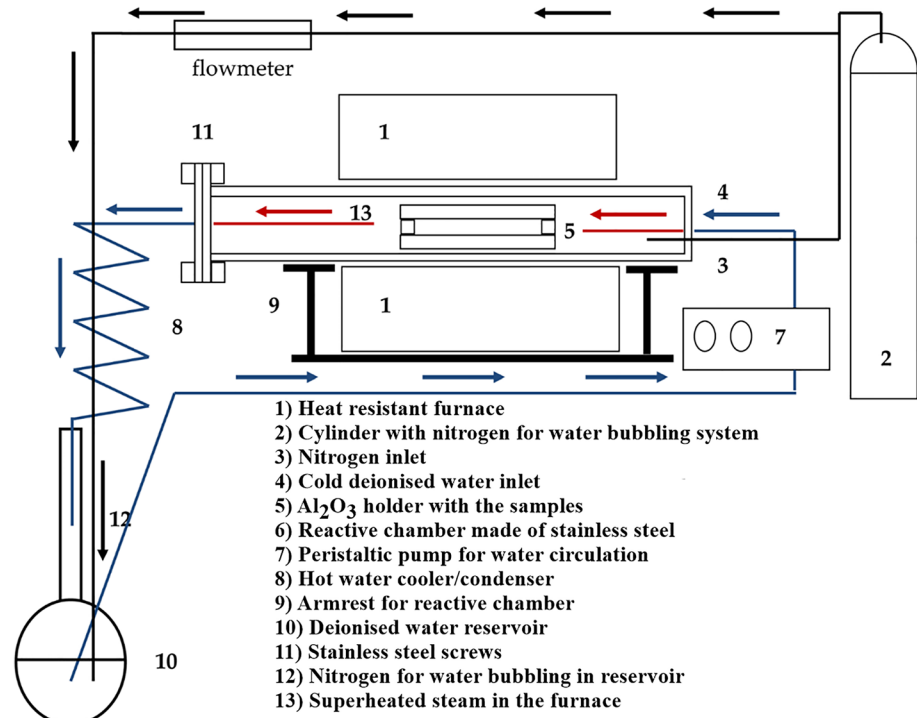
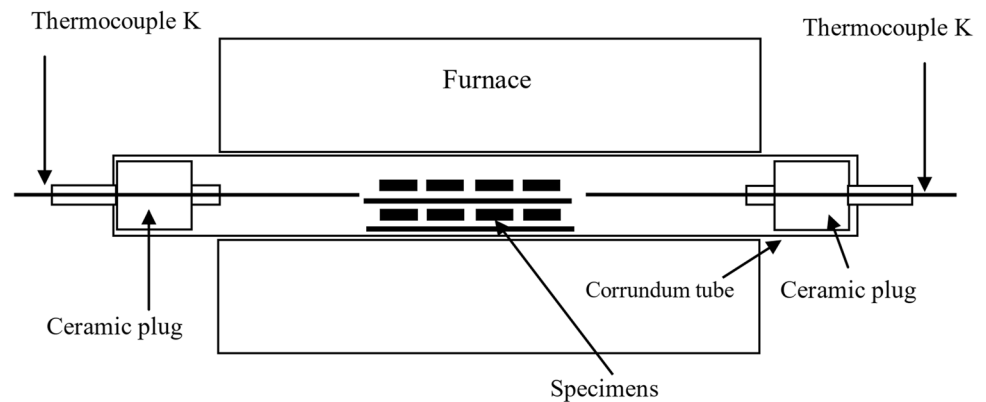


Fig. 2 Air oxidation rig used in this study

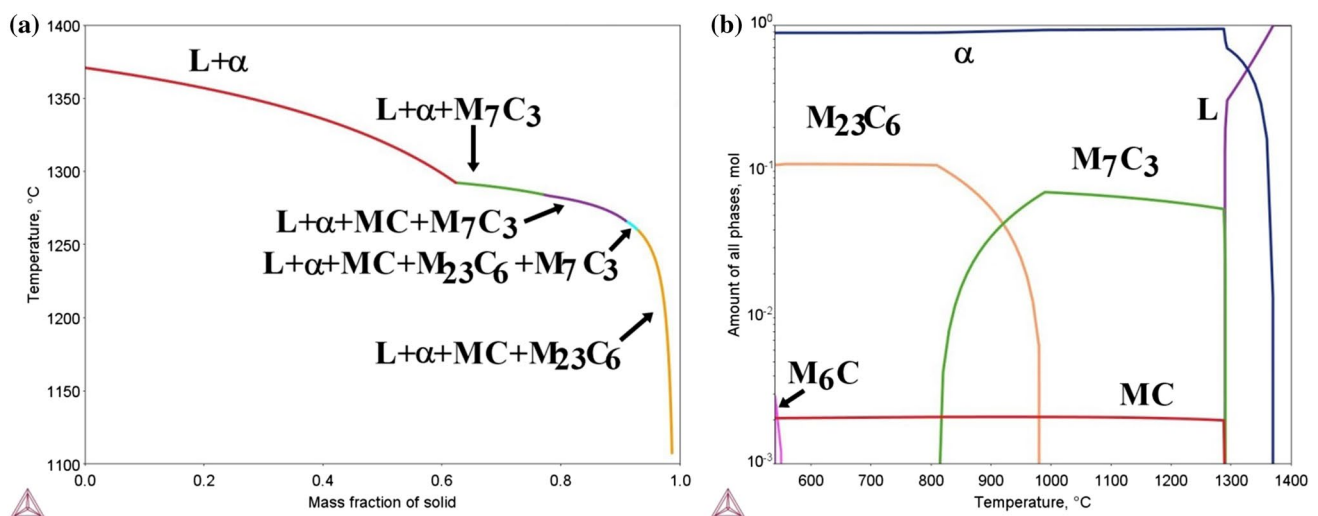
3 Results and discussion

3.1 Solidification simulation via the Scheil model and stability of the X-40 Co-based superalloy under equilibrium conditions

In Fig. 3a the solidification sequence predicted by the Scheil model is presented. It should be noted that the model took into consideration the segregation of alloying elements during solidification. The solidification path started at 1371 °C, with the crystallization of the α -phase. A gradual increase in the amount of α -phase was observed, following the temperature decrease to 1293 °C, with the fraction of solid (f_s) changing to 0.62. As solidification proceeded, the M_7C_3 starts to precipitate (f_s increase to 0.77), followed by MC carbide formation at 1283 °C. At 1266 °C, the final type of carbide, i.e. $M_{23}C_6$, begins to precipitate (f_s equal 0.9). M_7C_3 formation ends at 1260 °C, at f_s equal to 0.93. It was assumed that complete solidification occurs when the liquid

phase in the simulation is less than 1%, therefore here, X-40 Co-based superalloy solidification was calculated to end at 1107 °C. A similar approach in solidification process analysis was presented by Cao et al. [26]. Based on the obtained data, it can be concluded that the solidification sequence of the X-40 superalloy is as follows: $L \rightarrow L + \alpha$, $L + \alpha + M_7C_3$, $L + \alpha + MC + M_7C_3$, $L + \alpha + MC + M_{23}C_6 + M_7C_3$, $L + \alpha + MC + M_{23}C_6$.

A phase stability diagram (equilibrium conditions) was also prepared for the X-40 Co-based superalloy (Fig. 3b). It has been shown that the main strengthening phase in the intermediate temperatures is $M_{23}C_6$, with a mole fraction of 0.11. Additionally, the MC and M_6C carbides are present. The amount of $M_{23}C_6$ decreases at temperatures exceeding 810 °C, and the first M_7C_3 carbides appear. Above 918 °C, M_7C_3 is the main strengthening phase, with a maximum mole fraction of 0.07. The solvus temperature of $M_{23}C_6$ is 979 °C, whereas above 991 °C, the M_7C_3 carbides gradually start to dissolve. The MC carbides are relatively stable in the

**Fig. 3** a Scheil solidification simulation; b phase stability under equilibrium conditions in the X-40 Co-based superalloy

range of 600–1290 °C. The calculated incipient melting and liquidus temperatures are 1289 °C and 1371 °C, respectively.

3.2 X-40 superalloy as-cast microstructure characterization

XRD was performed to analyze the phase composition of the as-cast X-40 superalloy (Fig. 4). Two strong peaks, corresponding to the cobalt matrix (α), are visible, with the FCC structure ($Fm\text{-}3m$) [27] being registered. Additionally, the peaks originating from the M_7C_3 [28] and $M_{23}C_6$ [29] carbides were detected.

The microstructure of the X-40 Co-based superalloy is presented in Fig. 5. A typical dendritic structure is observed with second-phase precipitates located in the interdendritic spaces (Fig. 5a). Based on the image analysis, it was shown that the mean surface fraction of all precipitates is 10.1% ($\pm 1.6\%$). The strengthening precipitates are unevenly distributed in the casting (Fig. 5b). They are characterized by a varied morphology, from very complex shapes and elongated rectangular shapes to blocks with sharp edges. Such distribution and differences in the precipitates' morphology indicate segregation of the alloying elements during solidification. This was confirmed by calculating the partitioning coefficient (Fig. 5c). The dendritic regions are enriched in Co and Ni since k^{Co} and k^{Ni} are 1.06 and 1.08, respectively. Cr, W and Zr are dominant in the interdendritic spaces. Their segregation coefficients do not exceed 1. The lowest k value of 0.23 corresponds to Zr, which indicates its strong segregation into the interdendritic spaces.

Elemental distribution maps, shown in Fig. 6, indicate the enrichment of the interdendritic spaces in Cr, W and Zr. These elements form the precipitates that strengthen the α -matrix. The Cr-enriched areas correspond to the M_7C_3

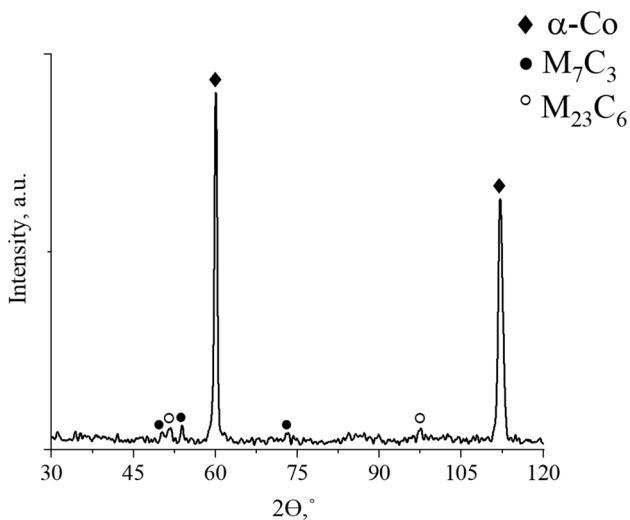


Fig. 4 XRD spectrum of the as-cast X-40 Co-based superalloy

carbide precipitates. Moreover, the differences in W concentration in the matrix surrounding the precipitates are revealed, which may indicate local differences in the chemical composition in the casting volume.

Closer observation of the Cr M_7C_3 carbides in SEM-BSE contrast revealed the presence of additional precipitates or bright layers at the edges (Fig. 7a). According to thermodynamical simulations, two Cr-rich carbides can be present in the X-40 superalloy, namely M_7C_3 and $M_{23}C_6$. The first one is stable at high temperatures, and the second at lower. The M_7C_3 carbides form at a low Cr/C concentration ratio, and it is metastable in the X-40 Co-based superalloy during high-temperature exposure. The decomposition of M_7C_3 to $M_{23}C_6$ can occur via an in situ reaction $23Cr_7C_3 = 7Cr_{23}C_6 + 27C$ and tend to form potent secondary carbides strengthening. The released C atoms locally diffuse into the matrix and can combine with Cr, allowing to form fine precipitates according to $6C + 23Cr = Cr_{23}C_6$. The formula of the $M_{23}C_6$ estimated with electron beam microprobe was presented as $Cr_{17}Co_4W_2C_6$, so a significant amount of Co occurs in this phase [30]. The local change in Cr concentration in region II (Fig. 7b) on the M_7C_3 carbide suggests that the primary $M_{23}C_6$ is present or the phase transformation $M_7C_3 \rightarrow M_{23}C_6$ started during the cooling of the cast. The cooling rate from melting temperature to 650 °C in a similar shell mold was measured by Matysiak et al. [31] and was equal 10–12 °C/min. It can suggest that the cooling rate in ceramic shell molds is very low, giving time for such transformations. Ghasemi et al. [22] indicated that the $M_7C_3 \rightarrow M_{23}C_6$ phase transformation takes place from the outer edges of the M_7C_3 carbide during solution heat-treatment, while in the MAR-M509 superalloy this transformation was observed in as-cast state after slow cooling [30].

STEM-EDX distribution maps of selected alloying elements in interdendritic regions are presented in Fig. 8. Selected area electron diffraction (SAED) was carried on the matrix, as well as on Cr, Zr- and W-rich precipitates. The SAED of the matrix (Fig. 9a) indicates that it has an FCC structure ($Fm\text{-}3m$) with a nominal lattice parameter of $a = 3.54 \text{ \AA}$ [27]. HCP-structured matrix areas were not found. The Cr-rich regions, i.e. M_7C_3 carbides, are characterized by a hexagonal ($P6_3mmc$) crystal structure (Fig. 9b), with nominal lattice parameters of $a = b = 13.938 \text{ \AA}$ and $c = 4.477 \text{ \AA}$ [28]. The areas with increased concentration of Zr (and also with W) are MC carbides (Fig. 9c) with a face-centered cubic crystal structure ($Fm\text{-}3m$) and lattice parameter of $a = 4.76 \text{ \AA}$ [32]. The crystal lattices representing the detected phases are shown in Fig. 9d.

It should be noted that the precipitate-free regions strongly enriched in W were additionally detected in our experiments (Fig. 6). Such W-rich areas cannot be attributed to incomplete diffusion or another solid phases since there is no interface with the γ matrix, as shown by STEM-HAADF.

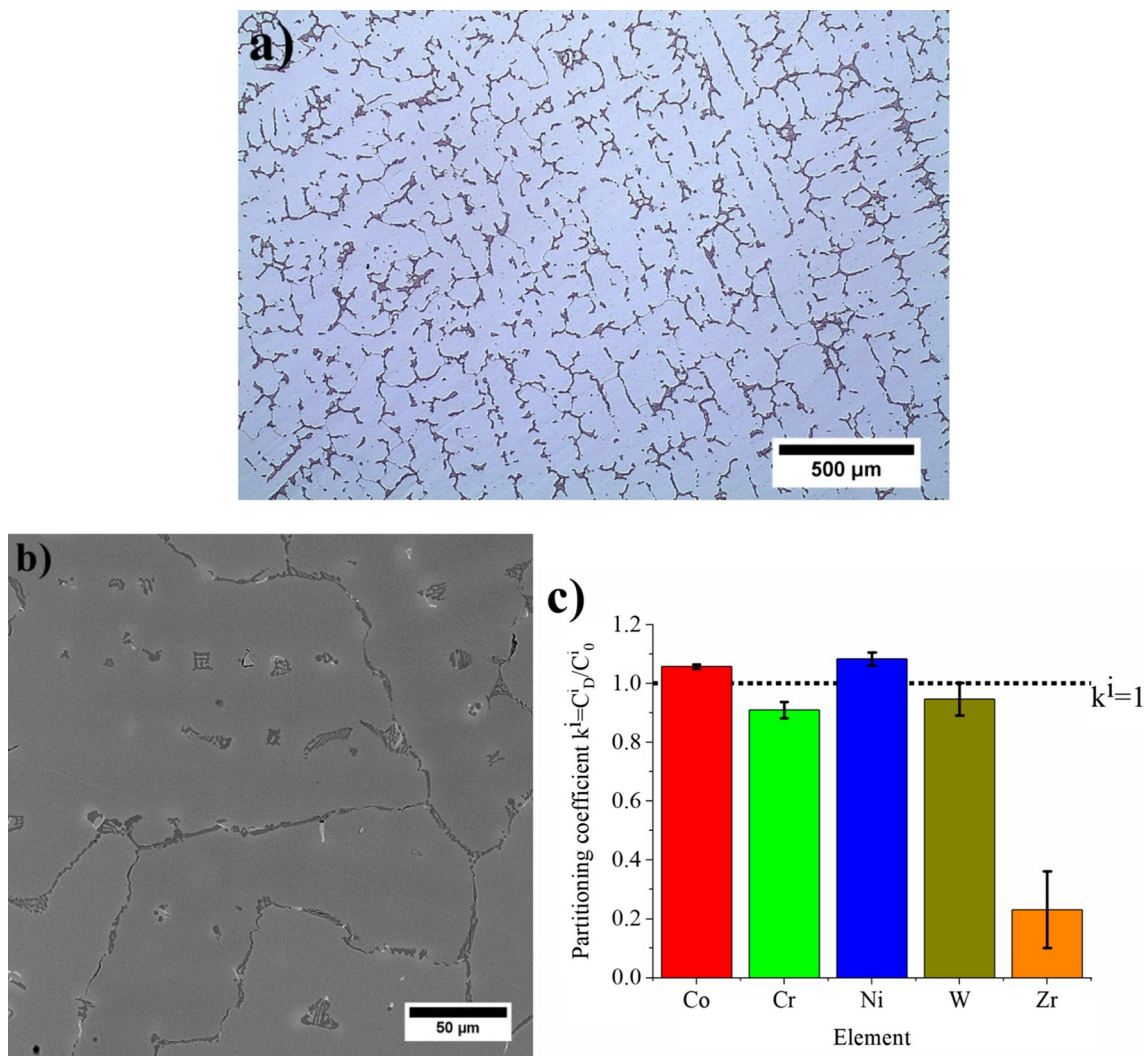


Fig. 5 **a** General microstructure of the X-40 Co-based superalloy, LM; **b** distribution and morphology of precipitates, SEM-BSE; **c** partitioning coefficient calculated based on the SEM-EDX measurements

Therefore, the formation can correspond to the enrichment of the residual liquid phase in W in the last stage of superalloy solidification. Similar results have been obtained by Guyard et al. [34], who stated, based on experiments on Stellite 6, that W concentration was higher in the liquid phase compared to solid phases. Tungsten, being very sluggish, hinders diffusion from the liquid into the matrix, and M_7C_3 carbides are not fully obtained using the usual cooling rates. Some residual liquid is retained by W supersaturation. The authors stated that undercooling of most as-cast Co-based alloys, like satellites, could be caused by the behavior of W. Hamar-Thibault et al. [35] detected M_6C carbides in regions enriched in W, induced by solidification segregation. Johansson and Uhrenius [36] proposed the following reaction that takes place during heat-treatment: matrix (high W) + carbon \rightarrow matrix (low W) + M_6C . Jiang et al. [37], based on the investigation of directionally solidified DZ40M superalloys,

suggested that after heat treatment, M_6C precipitates appear on the surface of M_7C_3 carbides adjacent MC carbides. The formation of the tungsten-rich M_6C was attributed to W segregation originating from phase transformation of the W-rich MC carbides and good lattice matching with the M_7C_3 . Considering the presented results and analysis, it can be concluded that in the X-40 superalloy, the above-described reaction and presence of M_6C precipitates are probable. Areas with increased sulfur content were also detected and are considered as contaminations. To obtain more information about these regions, additional STEM-EDX measurements were performed. A “core-shell” type morphology area was observed on the disclosed cross-section, i.e., a plate-like precipitate enclosed in MC carbide (Fig. 10). The plate-like precipitate is approx. 15–20 nm thick. Similar plate-like precipitates with an increased concentration of Zr and S are most likely carbide-sulphides $Zr_4S_2C_2$. Sims et al. [30] and

Fig. 6 Alloying elements distribution maps, SEM–EDX

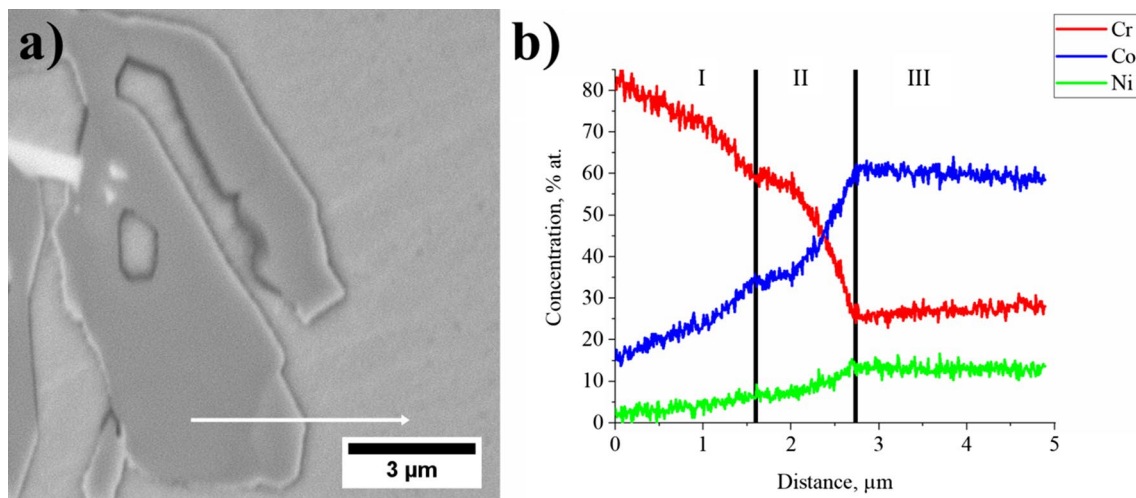
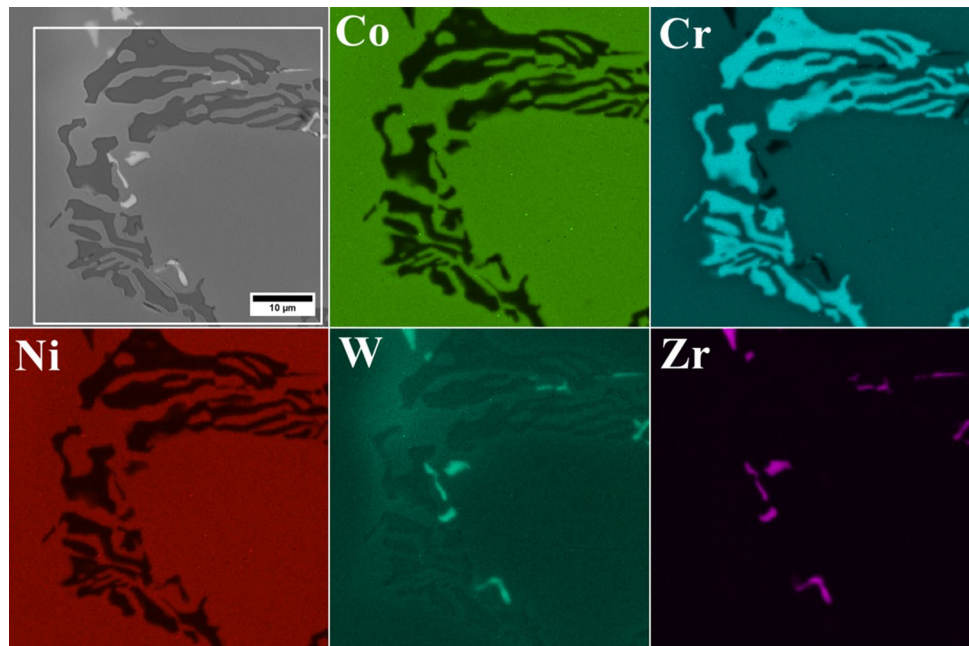


Fig. 7 **a** Morphology of the $M_{23}C_6$ (region II) carbide on the edge of M_7C_3 (region I) carbide, SEM-BSE; **b** distribution of the selected alloying elements in the precipitates and matrix. White arrow marks measurement direction, SEM-EDX

Xie et al. [38] confirmed the presence of $Zr_4S_2C_2$ in cast superalloys. Zr plays the role of a “getter” and minimizes the presence of elemental sulfur at the grain boundaries by creating $Zr_4C_2S_2$. According to the Co–S phase diagram, sulfur is insoluble in cobalt, so potential S segregation may lead to eutectic phase formation characterized by a low melting point. The presence of the liquid phase along grain boundaries broadens the solidification range, which may increase casting susceptibility to hot cracking during solidification.

Wallace et al. [39] stated that in cast alloys, precipitates form due to the segregation of sulfur and carbon to interdendritic spaces, and they increase in size and amount with slow

cooling from liquidus. The structure and chemistry of the $M_4C_2S_2$ phase were investigated by Kudielka and Rohde [40] in Fe-based alloys. They presented that sulfo-carbide has a hexagonal structure $P6_3/mmc$ with nominal lattice parameters of $a = 3.395 \text{ \AA}$ and $c = 12.11 \text{ \AA}$, when Zr is in the M position. Similar plate-like sulfo-carbide with adjacent M(C, N) precipitates have been observed in the IN713LC superalloy [39]. Chemically, a stoichiometric $M_4S_2C_2$ phase can be considered as an MC or M(C, N) phase, in which half of the carbon (or nitrogen) is replaced by sulfur. In this case, the following crystallographic relationship can occur $\langle 110 \rangle_{\text{Cubic}} \parallel \langle 11\bar{2}0 \rangle_{\text{Hexagonal}}$. The a_0 for the hexagonal

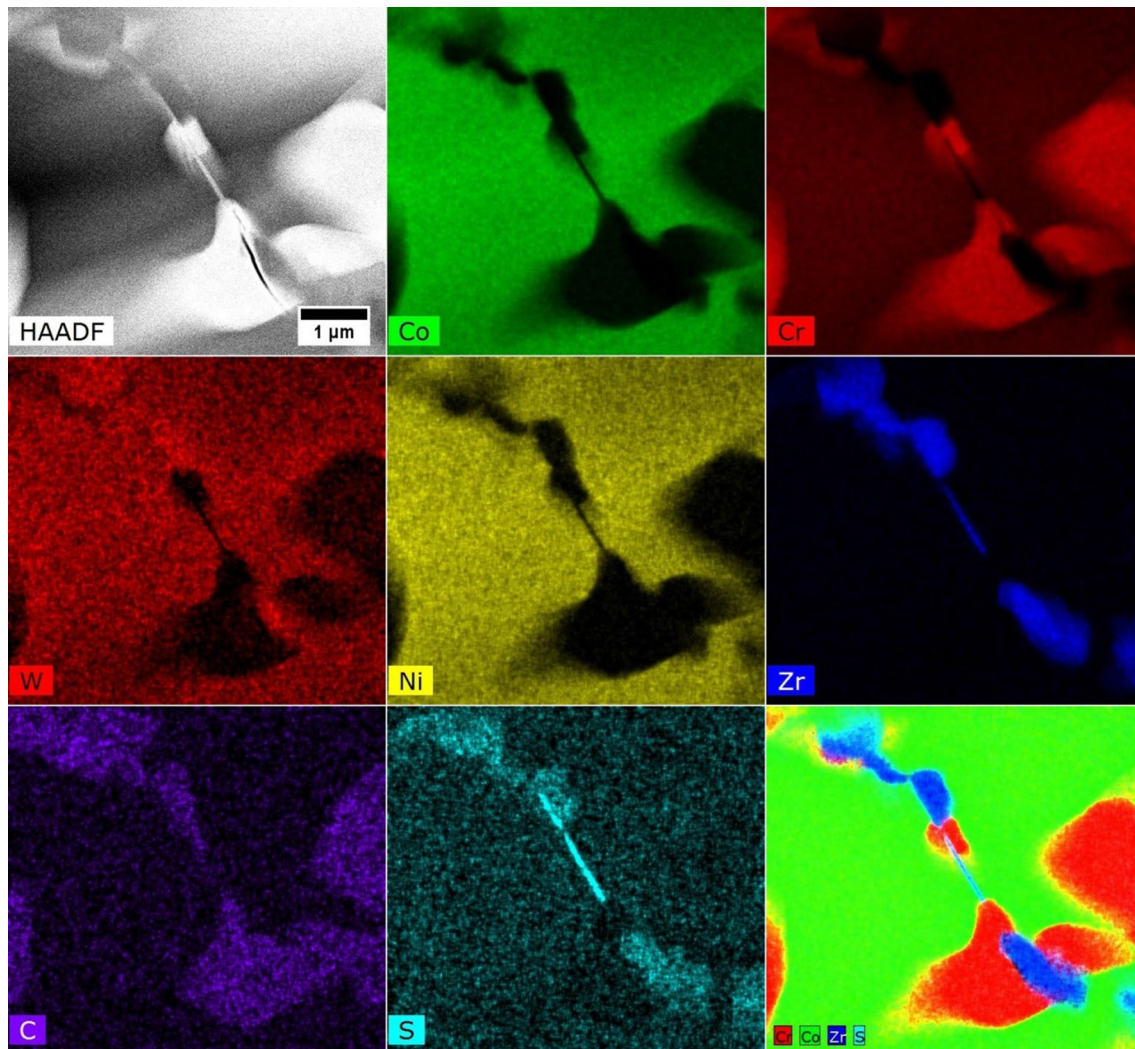


Fig. 8 Alloying elements distribution in the primary precipitates, STEM-EDX

structure is equal around $\sqrt{\frac{2a^2}{2}}$, whereas the $\sqrt{\frac{2a^2}{2}}$ calculated for Zr-rich M(C, N) in the IN713LC is 3.13 Å [39, 40]. It indicates that a crystallographic orientation relationship between MC carbides and $M_4S_2C_2$ sulfo-carbides is possible. The revealed “core-shell” morphology in the X-40 superalloy suggests that the misfit and coherency strain would be reduced if the Zr-rich layer of MC carbides ($ZrC = 4.69 \text{ \AA}$) precipitate on the sulfo-carbide ahead of the bulk (Zr, W)C.

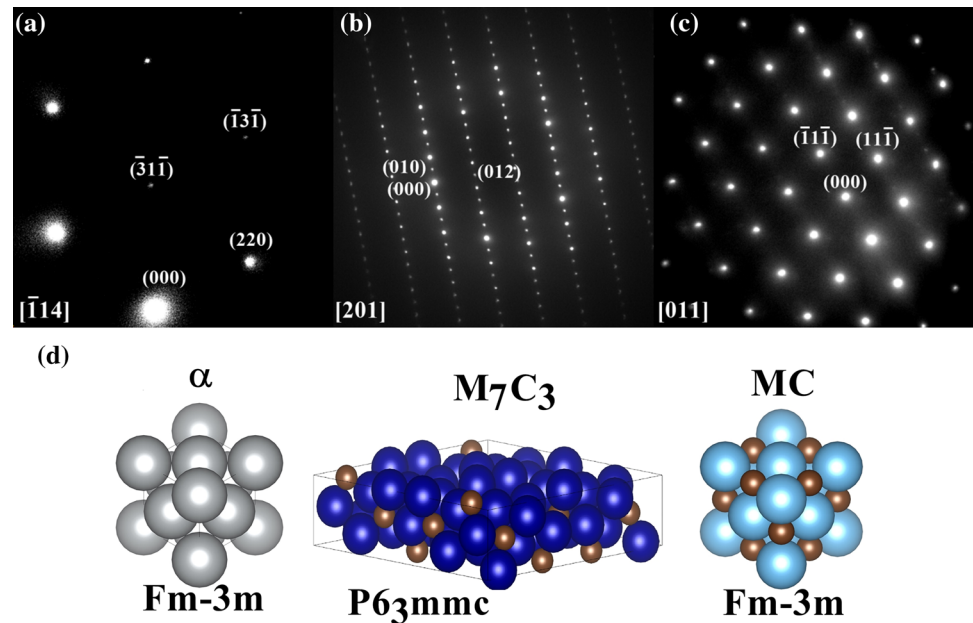
3.3 Analysis of the linear coefficient of thermal expansion by dilatometry

Figure 11 shows the change in specimen length (ΔL), linear coefficient of thermal expansion (α), and the change of active power with temperature (ΔP).

The first dilatation effect around 600–800 °C could be related to the formation of secondary phases from a

super-saturated matrix. Lobl and Tuma [41], based on annealing experiments ($T = 550\text{--}900 \text{ }^\circ\text{C}$, $t = 1\text{--}300 \text{ h}$) of the Co–28Cr–1.45C alloy, indicated that the amount of precipitated carbides with increasing temperature and holding time alloys tend to equilibrium, which is achieved fairly rapidly above 700 °C. The amount of carbides gradually increases with temperature and time to the peak at 750 °C. At higher temperatures, the amount of carbides decreases due to dissolution. The authors observed M_7C_3 and $M_{23}C_6$ carbides, whereas, at lower temperatures, the M_7C_3 carbides predominated. The diffusion activation energy calculated via Arrhenius’s equation (60–67 kcal/mol) suggests that the diffusion of Cr controls carbide precipitation. Consequently, at service temperatures further carbide precipitation can occur. It can lead to hardening after several hours or long-term exposure (depending on temperature), after which the coagulation of precipitates can also take place. The potential formation and presence of $M_{23}C_6$ need a short

Fig. 9 SAED pattern: **a** matrix; **b** M_7C_3 carbides; **c** MC carbides; **d** lattice structures of the detected phases calculated by Vesta [33]



clarification. Low interfacial energy of $M_{23}C_6$ with the α phase is connected with a good match across the interface [42]. The lattice parameter of the carbides is approximately three times higher than the matrix's, therefore, the misfit in the selected planes is tiny [43]. Nucleation of $M_{23}C_6$ is favorable, however, it is not a stable phase [44]. The second dilatation effect starts at approx. 950–1000 °C. This range coincides with the increase in active power, which also indicates a change in the magnetic permeability of the superalloy. This effect may originate from the phase transformation $M_7C_3 \rightarrow M_{23}C_6$ or/and precipitation of the second phase from the matrix. Hamar-Thibault et al. [34], based on experiments focusing on carbides transformation during ageing in cobalt alloys, stated that the tungsten necessary to build up $M_{12}C$ carbides is removed from the α phase. Simultaneously, the carbon concentration of the different primary carbides decreases after ageing, providing carbon to form new $M_{12}C$ carbides. During ageing, M_7C_3 decomposes and is replaced by M_6C , while the chemical composition of the latter evolves to $M_{12}C$. In the case of $M_{12}C$ carbides, the misfit with the matrix is approx. 2 pct, so nucleation is more difficult and will be referred to later. The Cr-rich M_7C_3 or/and $M_{23}C_6$ carbides tend to precipitate first, as the diffusion of W, required for M_6C carbide growth, is very low.

3.4 Analysis of phase transformation temperatures by DSC

The incipient melting (T_S) and liquidus (T_L) temperatures of the X-40 superalloy were determined during heating, with a rate of 10 K/min. It is equal to $T_S = 1405$ °C, $T_L = 1421$ °C, and the enthalpy of melting is 218 J/g (Fig. 12a). The DSC

curve shows the thermal effects of dissolving Cr-rich carbides and the dissolving of MC carbides at 1283 °C. Based on thermodynamic simulations, it was found that M_7C_3 carbides are characterized by lower stability and will transform first. The thermodynamical simulation predicts the phase transformation of M_7C_3 to $M_{23}C_6$, proven previously via electron microscopy. Some other reported experimental works suggest that this can also take place also during heating [22, 43, 44]. Considering this, the melting process of the primary M_7C_3 carbide can be that the M_7C_3 first undergoes a phase transformation into $M_{23}C_6$ and then melts, instead of directly melting.

The analysis of DSC curves recorded during cooling (10 K/min) was performed to determine the liquidus and solidus temperatures, and the enthalpy of solidification (Fig. 12b). Due to overheating and subsequent undercooling, the phase transition temperatures obtained from the cooling curve are lower than those obtained from the heating curve. The first exothermic effect (1.6 J/g) is observed at 1393 °C and is probably related to the formation of primary carbides. The solidification process of the α dendrites and precipitates of the eutectic M_7C_3 carbides starts at 1366 °C. The solidus temperature designated as the extrapolated end of the exothermic peak (endset) is equal to 1365 °C. The enthalpy of solidification of the X-40 superalloy determined in the tests (217.1 J/g) is comparable with the enthalpy recorded during melting (218 J/g). The solidification process of the X-40 superalloy occurs in a very narrow temperature range, which results from the supercooling. The degree of supercooling depends on the cooling rate and the sample's mass. Small samples undergo significant supercooling due to small amounts of crystallization nuclei, which causes that

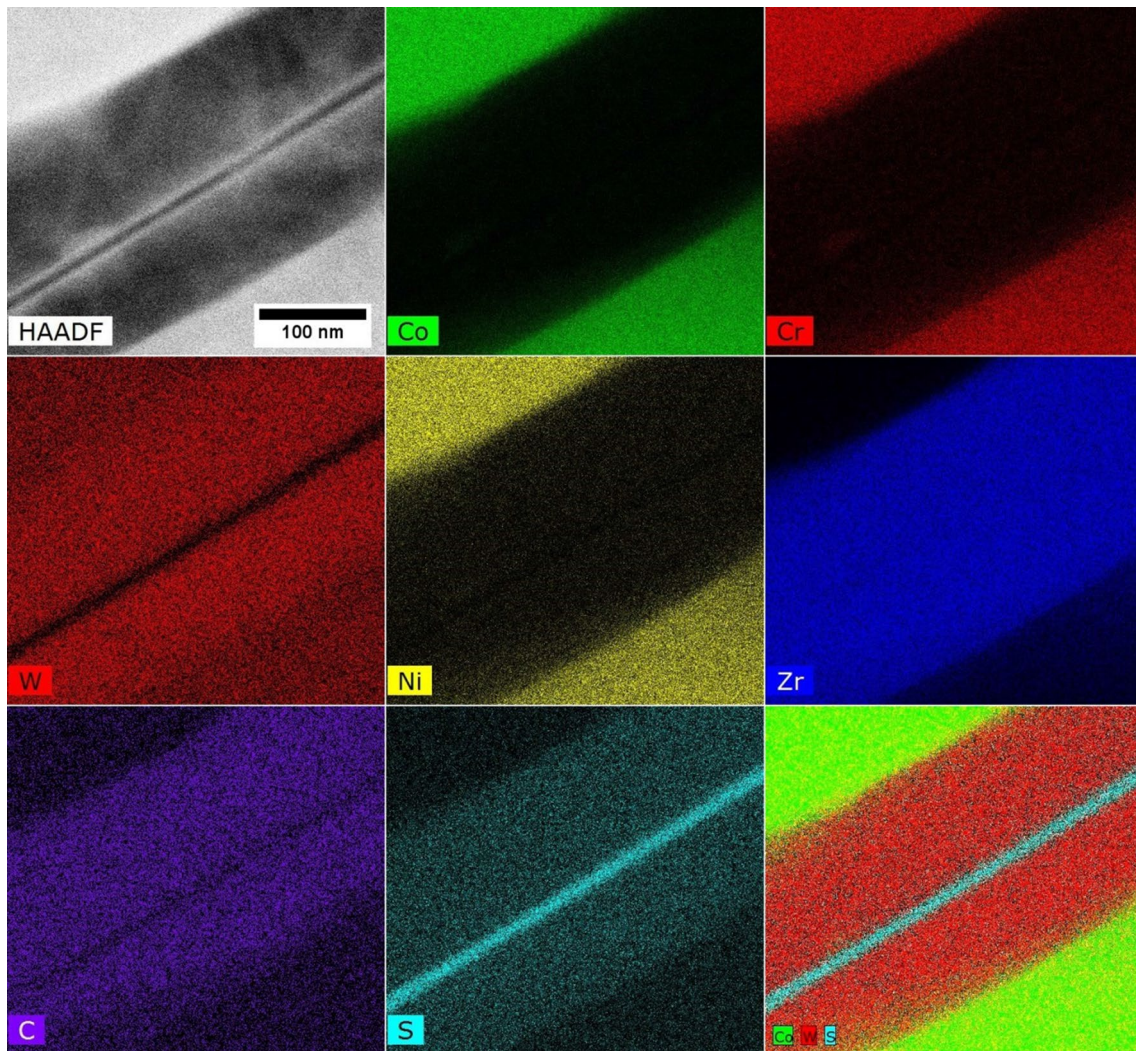


Fig. 10 Distribution of the alloying elements in the selected region with a “core–shell” morphology, STEM-HAADF

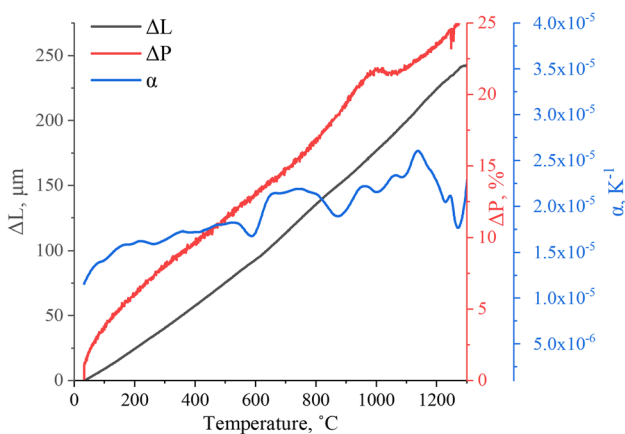


Fig. 11 Change of the specimen length, active power and linear coefficient of thermal expansion with temperature

the recorded freezing points differ from the equilibrium temperatures or those recorded during heating [50]. Therefore, the superalloy solidification temperatures obtained in the tests are closely related to the adopted measurement conditions, especially the cooling rate.

3.5 Corrosion resistance in the air and steam

The X-40 cobalt superalloy is directly used in the aerospace industry in the as-cast condition. One of the most important requirements during operation is appropriately high corrosion resistance, therefore the as-cast superalloy was exposed to corrosion tests in steam and air. In this work, two samples with the same surface finishing (600 SiC) were exposed. The mass gain of the X-40 Co-based superalloy samples increased with exposure time, while the mass gain rate decreased gradually with time (Fig. 13).

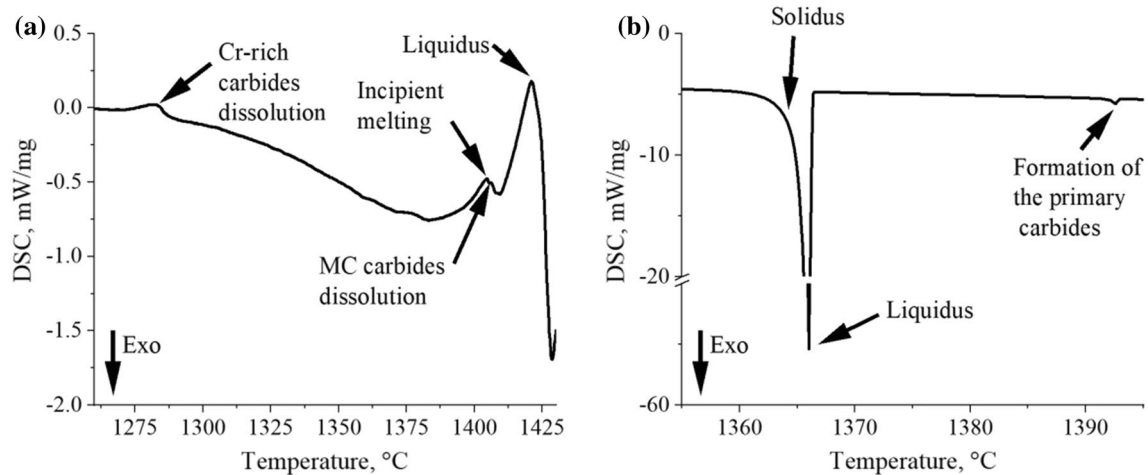


Fig. 12 DSC curve of the X-40 Co-based superalloy: **a** on heating; **b** on cooling

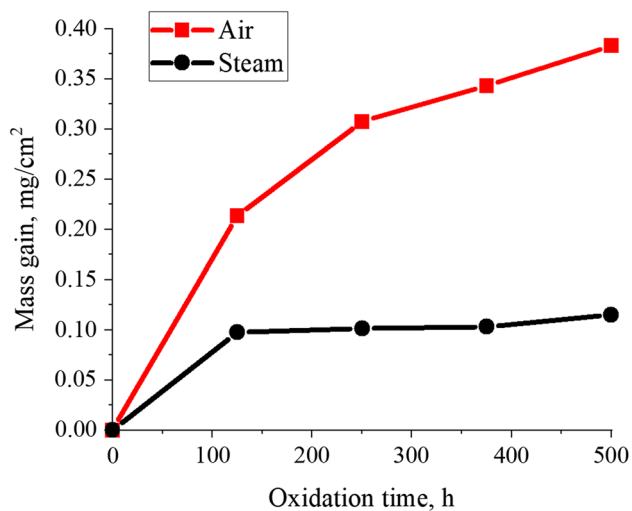


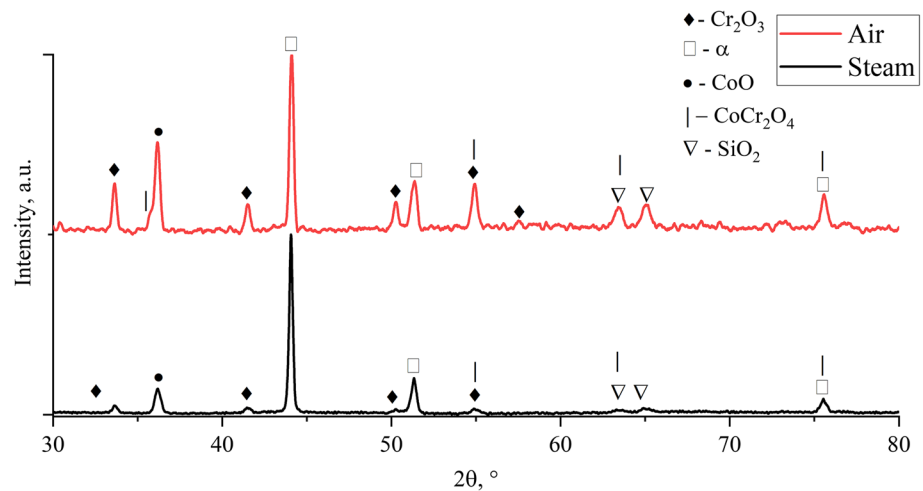
Fig. 13 Mass gain of the X-40 superalloy during cyclic-oxidation at 860 °C for 500 h in air and steam

The results suggest the formation of a protective oxide scale on both samples during the high-temperature oxidation in both environments, with no spallation or chipping of the oxide scale being found. The X-40 Co-based superalloy exposed to air showed a much higher mass gain than the sample exposed to steam. These results indicate that higher oxygen activity was found in the air than in steam, leading to the formation of a thicker oxide scale developed on the X-40 Co-superalloy. The calculated “ n ” exponent factor indicated that the sample exposed to air showed a close to parabolic rate constant behavior, where $n=0.4$, whereas the sample exposed to steam atmosphere showed $n=0.1$. The low “ n ” factor value means that in the case of the steam oxidation process, the oxide scale growth is completely slowed down. This can be attributed to low oxygen activity in steam due to

the very low steam flow (2.833 ml/min). In contrast, constant access to oxygen from the ambient atmosphere was present in the air, leading to the formation of a thicker oxide scale. The situation can be rationalized by the fact that there is no need to break the water molecule during air oxidation, whereas in steam it is required to release oxygen to form the oxide. Hence, this process consumes the time necessary to contribute to oxide scale formation. This situation contradicts the results presented by Archana et al. [51]. The researchers found that the mass gain of the exposed Ni-based alloy in steam was higher than that in air and followed a parabolic rate law for both atmospheres. Similar results in the case of low Cr boiler steels over the temperature range 500–700 °C have been described in literature [52]. The data inform that the air oxidation process is at least three times slower for low Cr steels than that for steam oxidation. In general, Co-based alloys oxidized in the air follow a parabolic rate in the temperature range 800–1100 °C, according to work presented by Buscail et al. [53]. There are no results related to steam oxidation behavior, therefore a comparison is not possible. However, the results achieved from air oxidation work are in good agreement with the previously mentioned studies. Figure 14 presents XRD analyses of the samples after exposure to steam and air at 860 °C for 500 h.

The oxide scale of the superalloy’s surface mainly consists of Cr_2O_3 , CoCr_2O_4 , CoO , and SiO_2 after both oxidation exposures. However, some distinct differences can be seen between the samples exposed to steam and air. A strong peak from the α -substrate is observed in both cases, suggesting a thin oxide scale. That situation is confirmed by the kinetic data presented in this work. Furthermore, the more intense peaks from Cr_2O_3 , CoO , SiO_2 , and CoCr_2O_4 are observed in the sample exposed to air, which was also confirmed by kinetic data, as higher mass gain in the air was attributed to a thicker oxide scale. A thicker oxide scale indicates more

Fig. 14 XRD spectrum of the X-40 Co-based superalloy after oxidation exposure at 860 °C for 500 h



oxygen diffused inwards into the material than in the case of the steam process. As previously mentioned, the 600SiC surface finish plays an important role in distributing more Cr from the metal matrix to the surface from the subsurface regions.

The surface microstructure of both samples after isothermal oxidation at 860 °C for 500 h in air and steam are shown in Fig. 15. The images were captured in BSE mode for both samples. There are visible morphology differences between the surfaces exposed to air and steam. The air process produced an oxide scale with larger grains (round and globular in size) than that observed for the steam-induced corrosion, where thin long grains, with a dimension of $1 \times 3 \mu\text{m}$ are present. In both cases, no crack delamination was found, suggesting good adhesion between the formed scale and the X-40 Co-based substrate.

The SEM–EDX measurements were carried out on the outer surface of the oxide scales to determine and compare their chemical composition (Fig. 16). It was observed that Cr is the main alloying element in the oxide layer found for both atmospheres, with the difference between the two almost negligible. Slightly more Co was found in the steam-induced oxide, similarly as for Ni and Si. The highest difference in element concentration within the oxide scale was found for Al, where considerably more was detected in the steam-induced oxide. In general, steam atmosphere develops a scale on X-40 Co-based superalloy richer in elements than observed for the air sample with the highest variation of Al.

Comparing those results with the XRD analysis and semi-quantitative chemical composition analysis, it can be concluded that the Cr_2O_3 precipitates are dominant in the oxide scale. The formation of the external oxide scale is a result of outward diffusion of Cr, Co and Ni in the highest rates. The other alloying elements either underwent internal oxidation, as XRD did not show evidence of Al-based phases within the oxide scale, or formed locally where XRD analysis could

not reach those particular phases. SEM–BSE images were taken of the exposed materials (Fig. 17). The oxide scale formed in the air has a thickness of 3–7 μm , while the one formed in steam was thinner in the range of 2–4 μm , as Fig. 17 shows. These findings are in good agreement with the kinetic data, where the material exposed to air showed a higher mass gain than the material exposed to steam. Both materials exposed to a rich oxygen atmosphere underwent internal oxidation. The measured internal oxidation depth reached 25 μm and 35 μm for air and steam, respectively. This may lead to further conclusions that the oxide scale formed on the sample exposed to steam showed the formation of a more porous scale than the oxide scale formed in the air. As previously mentioned, mainly Cr_2O_3 , CoCr_2O_4 , CoO , and SiO_2 formed in both samples.

Linear measurements of the alloying element distribution were performed via SEM–EDX on the selected regions of the air-induced oxide scale (Fig. 18).

Based on the analysis seen in Fig. 18a and b, it was revealed that close to the outer surface (area I), besides a high concentration of Cr, a high concentration of Co is observed (1 μm thick). This may indicate the presence of Cr_2O_3 and CoO and/or a CoCr_2O_4 spinel near the outermost surface. Furthermore, both phases were detected by XRD analysis. The area with a high Cr concentration (area II) contains Cr_2O_3 , whereas a dark-contrasted precipitate is present between the oxide scale and the substrate (area III). The SEM–EDX results indicate the presence of a Si region, suggesting SiO_2 formation. Figure 18c and d shows the change in chemical composition profile from the matrix and into the oxide, with visible dark-contrasted fine precipitates visible in area II. The analysis showed a high Co concentration corresponding to the matrix, while the region consists mainly of Cr associated with the formation of the Cr_2O_3 phase. Inside the oxide, about 2.5 μm from the beginning of the measuring line (dark precipitate), a local increase in Cr

Fig. 15 Microstructure of the oxide scale on the X-40 Co-based superalloy after oxidation at 860 °C for 500 h in: **a-b** air; **c-d** steam at high temperature

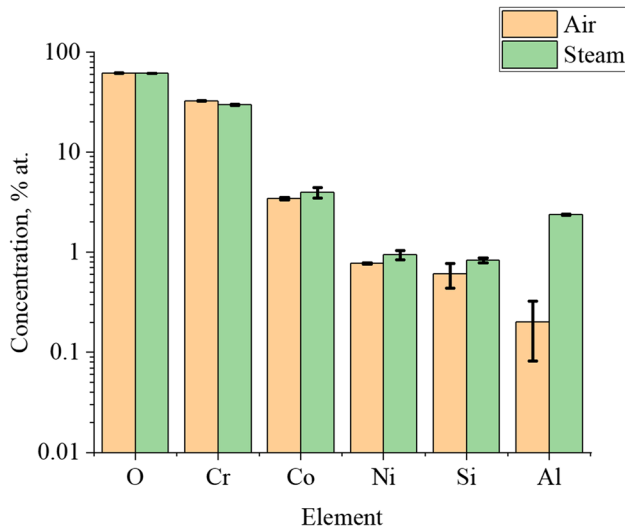
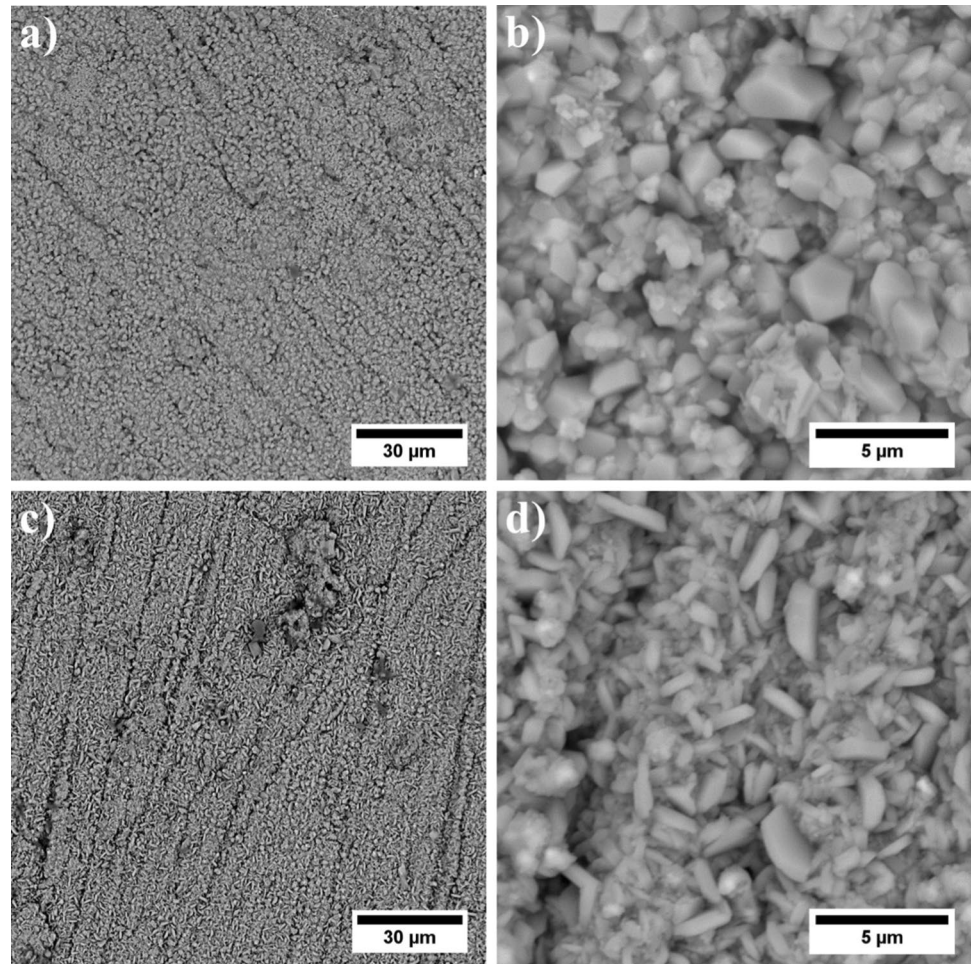


Fig. 16 Results of the semi-quantitative SEM-EDX analysis of the oxide scales' chemical composition

concentration and a simultaneous decrease in O concentration was observed. This finding may correspond to residual precipitates of Cr-rich carbides. Figure 18e and f shows the analysis from the matrix and across small block-shaped precipitates (bright contrast), with a core-shell morphology. The fine precipitate was enriched in W, corresponding to a carbide, probably MC or possibly M_6C . The Co concentration gradually decreased with simultaneous Cr content enrichment until the shell's core was reached. Moreover, an increase in Zr concentration was observed (bright contrast). The elongated precipitate with a high Zr concentration may indicate the residual sulfo-carbide phase revealed during the base material study. In Fig. 19, similar to air-oxidized samples, the steam-oxidized samples underwent detailed SEM investigations with EDX line scan analyses in three different locations.

The results presented in Fig. 19a and b clearly show the region is enriched in Cr and O, suggesting the formation of a protective Cr_2O_3 phase. Furthermore, a darker precipitate was observed between the oxide scale and substrate with increasing Si concentration (SiO_2). Additionally, a slight increase in Al content was found in this region. The presence

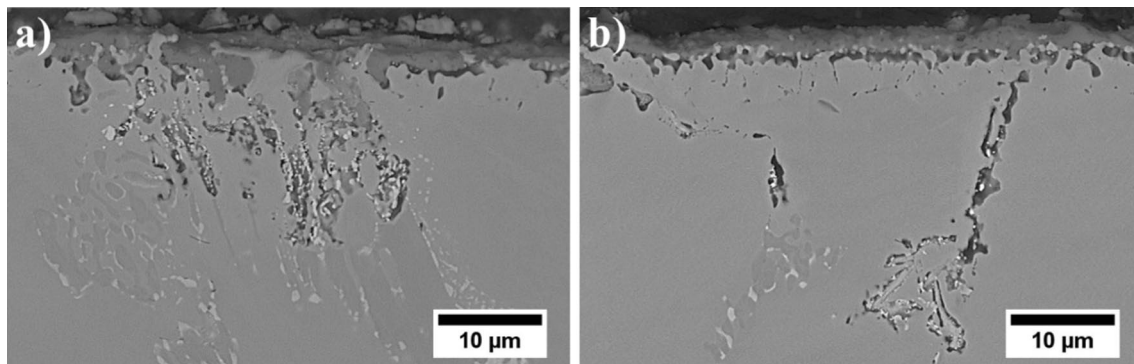


Fig. 17 Cross-section microstructure of the X-40 superalloy after oxidation in: **a** air; **b** steam, SEM-BSE

of Al in the oxide scale may lead to the conclusion that the X-40 Co-based alloy develops an oxide enriched with Al. Previous works [20, 54] indicate that the simultaneous presence of Cr and Al increases the oxidation resistance of Co through the formation of an inner Al_2O_3 thin layer adjacent to the bulk metal and an outer layer consisting of Cr_2O_3 . The formation of a stable Al_2O_3 layer occurs only if the Al content exceeds a minimum value, below which internal oxidation is observed. Some regions in the X-40 Co-based superalloy are enriched in Al which suggests that a local internal Al_2O_3 phase could be present. In Fig. 19c and d, the oxide scale's outer layer possesses higher Cr and Si concentrations. The changed phase-contrast in the SEM-BSE image suggests chemical composition fluctuations. The image reveals the interlayer dividing the oxide scale and the matrix. The last analysis (Fig. 19e and f) was conducted in a precipitate with dark contrast several microns below the oxide scale. This precipitate has a thickness exceeding $2\ \mu\text{m}$ with a strong Si and O concentration, suggesting SiO_2 phase development.

4 Conclusions

Microstructure observations of the as-cast X-40 Co-based superalloy and analysis of its selected properties at high temperatures were performed. The main conclusions of this study are the following:

- The microstructure of the as-cast X-40 Co-based superalloy is mainly controlled by the formation of primary solid solution α dendrites and the segregation of carbon and alloying elements into the interdendritic regions to form MC, M_7C_3 and M_{23}C_6 carbides. Locally, plate-like $\text{Zr}_4\text{S}_2\text{C}_2$ sulfo-carbides have been identified.
- In general, the primary structure of cast X-40 Co-based superalloys is locally out of thermodynamic equilibrium, and subsequent heat treatment or long-term service may induce carbide transformation. Based on the differences in coefficient of thermal expansion, the precipitation of Cr-rich carbides from the matrix may occur between 650 and 750 °C.
- The dissolution effect from Cr-rich carbides was detected on the DSC curve around 1283 °C, while from the MC carbides at around 1406 °C.
- The high Cr content in the X-40 superalloy and the relatively low temperature of 860 °C are thought to be favorable for the preferential formation of a stable Cr_2O_3 layer both in air and steam.
- After 500 h of exposure to steam at 860 °C, the mass gain was $0.11473\ \text{mg}/\text{cm}^2$, whereas to air the mass gain was three times higher at $0.38298\ \text{mg}/\text{cm}^2$

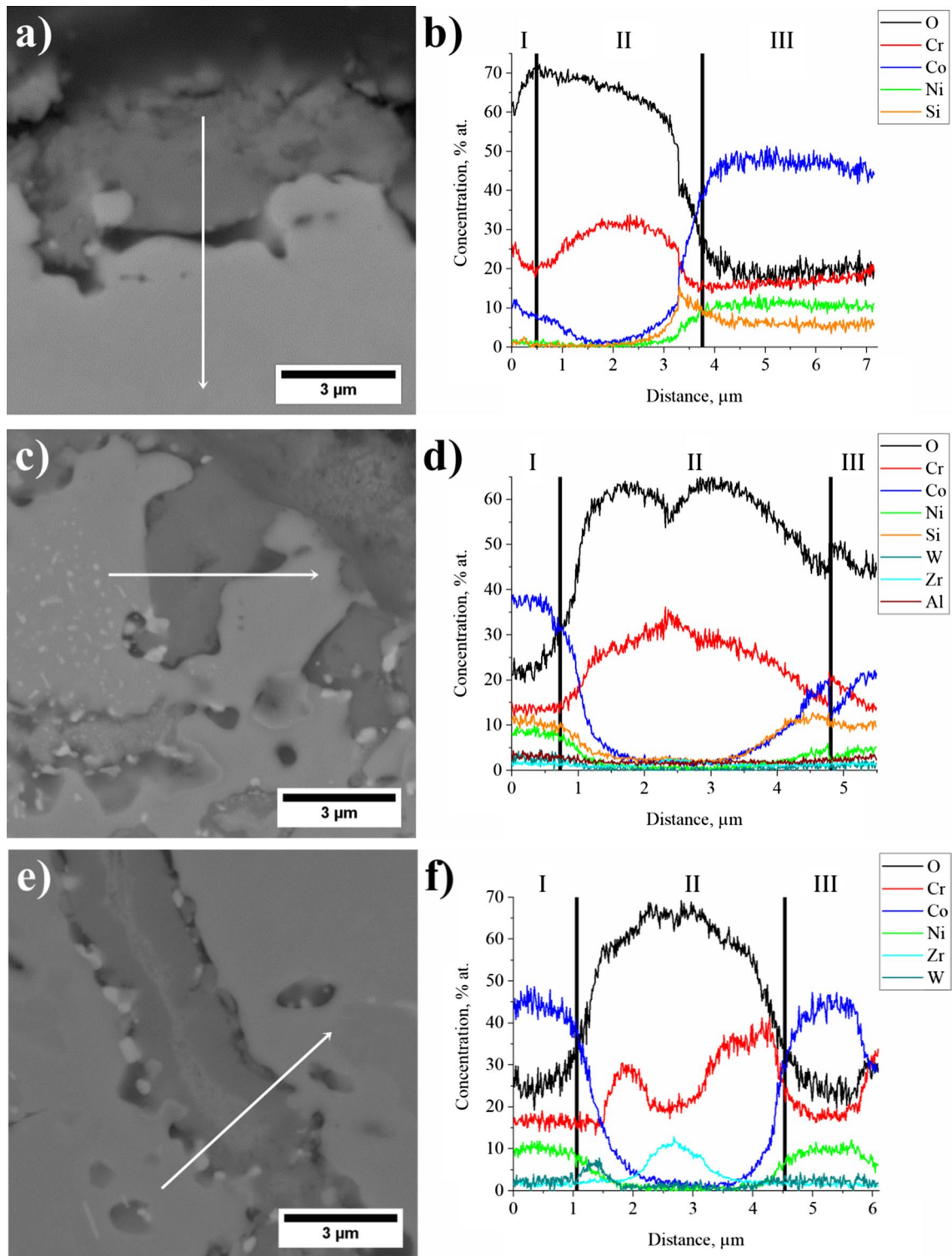


Fig. 18 a–f Distribution of the selected alloying elements in the oxide scale (air). White arrows mark measurement direction, SEM–EDX

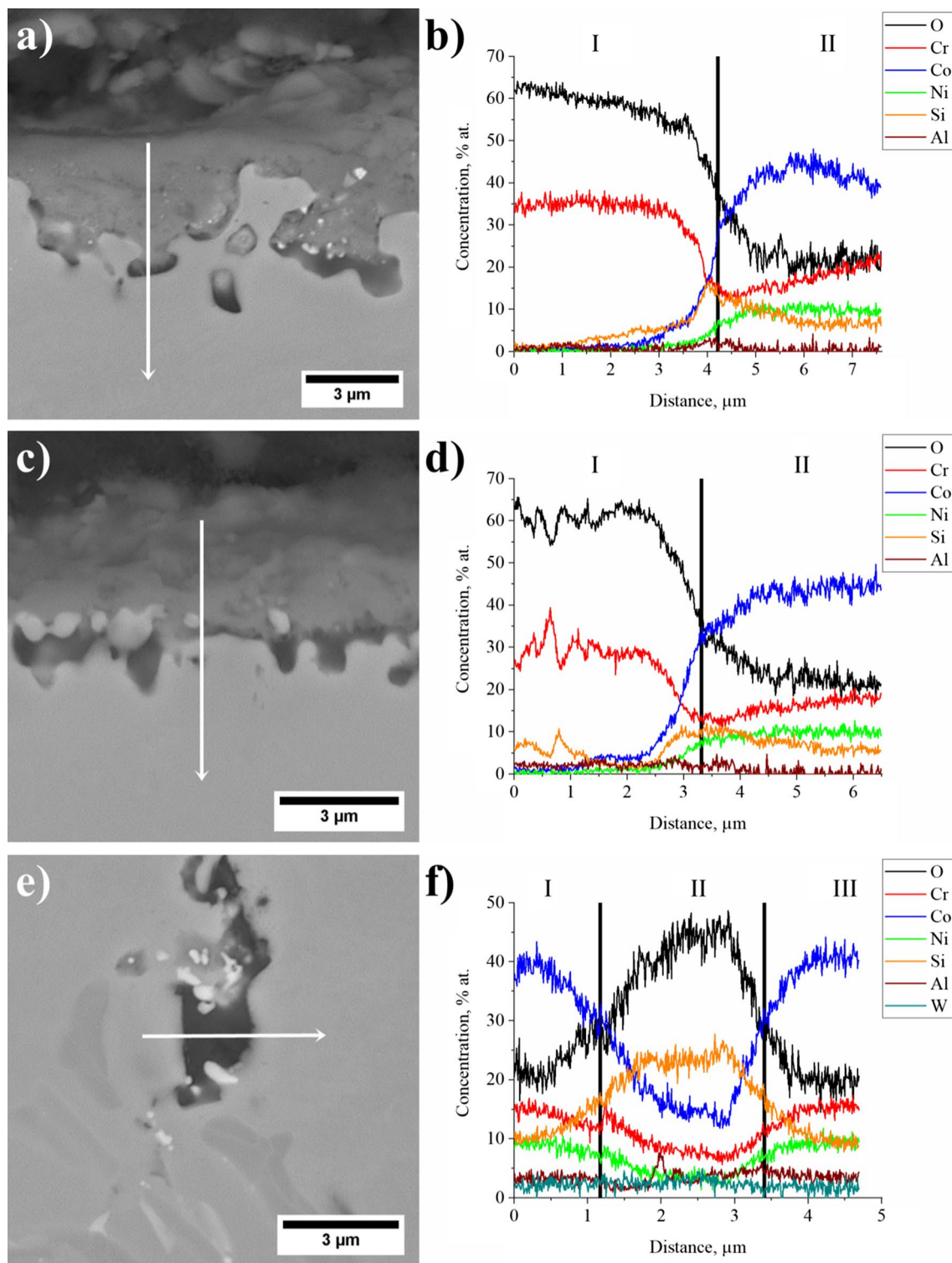


Fig. 19 a–f Distribution of the selected alloying elements in the oxide scale (steam). White arrows mark measurement direction, SEM–EDX

Acknowledgements The authors gratefully acknowledge the funding by National Centre for Research and Development, Poland, under grant POIR.01.01.01-00-0631/18. The oxidation resistance experiments were supported by the Polish National Science Centre (Preludium 14)

under the grant for young scientists (M.G.R.) 2017/27/N/ST8/01801. M.G.R. thanks the European Virtual Institute on Knowledge-based Multifunctional Materials (KMM-VIN) for the fellowship to spend a research period at the Institute of Materials Research, Slovak Academy

of Sciences. O.M. was supported by the Scientific Grant Agency under contract VEGA project No. 2/0086/22.

Declarations

Conflict of interest The authors declare that they have no known competing financial interests or personal relationships that could have appeared to influence the work reported in this paper.

Ethical approval This article does not contain any studies with human participants or animals performed by any of the authors.

References

- Davies J. ASM specialty handbook. Heat-resistant materials. ASM International: Metals Park; 1997.
- Klastrom D. Wrought cobalt-base superalloys. *J Mater Eng Perform.* 1993;2:523–30. <https://doi.org/10.1007/BF02661736>.
- Coutsouradis D, Habraken L. Metallurgical applications of cobalt: a critical review. *J Met.* 1983;35:40–7. <https://doi.org/10.1007/BF03338183>.
- Singh K. Advanced materials for land based gas turbines. *Trans Indian Inst Met.* 2014;67(5):601–15. <https://doi.org/10.1007/s12666-014-0398-3>.
- Keyvani M, Garcin T, Fabregue D, Militzer M, Yamanaka K, Chiba A. Continuous measurements of recrystallization and grain growth in cobalt super alloys. *Metall Mater Trans A.* 2017;48:2363–74. <https://doi.org/10.1007/s11661-017-4027-8>.
- Rahmani K, Torabian A. Influence of welding on low cycle fatigue properties of Co-based superalloy FSX-414. *Trans Non-ferrous Met Soc China.* 2016;26:1326–35.
- Sims C. A history of superalloy metallurgy for superalloy metallurgists. In: Proceedings of the fifth international symposium on superalloys sponsored by the high temperature alloys Committee of the Metallurgical Society of AIME. Seven Springs, Pennsylvania, USA. October 7–11, 1984
- Tomaszewska A, Mikuszewski T, Moskal G, Migas D. Primary microstructure, microsegregation and precipitates characterization of an as-cast new type γ - γ' Co-Al-Mo-Nb cobalt-based superalloy. *J All Comp.* 2018;750:741–9. <https://doi.org/10.1016/j.jallcom.2018.03.397>.
- Shirpay M, Kazempour-Liacy H. Failure analysis of a repaired gas turbine nozzle. *J Fail Anal Prev.* 2013;13:243–8. <https://doi.org/10.1007/s11668-013-9667-4>.
- Kuzucu V, Ceylan M, Celik H, Aksoy I. Microstructure and phase analyses of stellite 6 plus 6 wt.% Mo alloy. *J Mater Proc Technol.* 1997;69:257–63. [https://doi.org/10.1016/S0924-0136\(97\)00027-7](https://doi.org/10.1016/S0924-0136(97)00027-7).
- Naalchian M, Kasiri-Asgarani M, Shamanian M, Bakhtiari R, Bakhsheshi-Rad H. Comprehensive microstructural investigation during dissimilar transient liquid phase bonding cobalt-based superalloys by BNi-9 amorphous interlayer foil. *J Mater Res Technol.* 2021;13:2144–60. <https://doi.org/10.1016/j.jmrt.2021.05.069>.
- Kuzucu V, Ceylan M, Celik H, Aksoy I. An investigation of stellite-6 alloy containing 5.0 wt% silicon. *J Mater Proc Technol.* 1998;79:47–51. [https://doi.org/10.1016/S0924-0136\(97\)00452-4](https://doi.org/10.1016/S0924-0136(97)00452-4).
- Szala J, Szczotok A, Richter J, Cwajna J, Maciejny A. Selection of methods for etching carbides in MAR-M509 cobalt-base superalloy and acquisition of their images. *Mat Charact.* 2006;56(4–5):325–35. <https://doi.org/10.1016/j.matchar.2005.11.015>.
- Luna Ramirez A, Porcayo-Calderon J, Mazur Z, Salinas-Bravo V, Martinez-Gomez L. Microstructural changes during high temperature service of a cobalt-based superalloy first stage nozzle. *Adv Mater Sci Eng.* 2016;2016:1745839. <https://doi.org/10.1155/2016/1745839>.
- Rakoczy Ł, Rutkowski B, Grudzień-Rakoczy M, Cygan R, Ratuszek W, Zielińska-Lipiec A. Analysis of γ' precipitates, carbides and nano-borides in heat-treated Ni-based superalloy using SEM, STEM-EDX and HRSTEM. *Materials.* 2020;13(19):4452. <https://doi.org/10.3390/ma13194452>.
- Kuzucu V, Ceylan M, Celik H, Aksoy I. Phase investigation of a cobalt base alloy containing Cr, Ni, W and C. *J Mater Proc Technol.* 1998;74:137–41. [https://doi.org/10.1016/S0924-0136\(97\)00261-6](https://doi.org/10.1016/S0924-0136(97)00261-6).
- Zhao Y, Zhang Y, Zhang Y, Luo Y, Tang D, Liu H, Fu H. Deformation behavior and creep properties of Co–Al–W-based superalloys: a review. *Prog Nat Sci Mater Int.* 2021;31:641–8. <https://doi.org/10.1016/j.pnsc.2021.09.009>.
- Coutsouradis D, Davin A, Lamberigts M. Cobalt-based superalloys for applications in gas turbines. *Mater Sci Eng.* 1987;88:11–9. [https://doi.org/10.1016/0025-5416\(87\)90061-9](https://doi.org/10.1016/0025-5416(87)90061-9).
- Sato J, Omori T, Oikawa K, Ohnuma I, Kainuma R, Ishida K. Cobalt-base high-temperature alloys. *Science.* 2006;312:90–1. <https://doi.org/10.1126/science.1121738>.
- Kamma R, Sakaguchi M, Okazaki M, Shimoda Y, Uchiyama T, Ochiai H, Watanabe M. Fatigue properties of alloy 718 overlay-coated with a Co-based X40 alloy by the micro spark coating. *J Sol Mech Mater Eng.* 2012;6(3):227–40. <https://doi.org/10.1299/jmmp.6.227>.
- Schoonbaert S, Huang X. Brazing and wide gap repair of X-40 using Ni-base alloys. *J Eng Gas Turb Power.* 2008;130:032101. <https://doi.org/10.1115/1.2836743>.
- Ghasemi A, Kolagar A, Pouranvari M. From as-cast to heat treated X-40 superalloy: effect of cooling rate after partial solution treatment on microstructural evolutions and mechanical properties. *Mater Sci Eng.* 2021;808:40891. <https://doi.org/10.1016/j.msea.2021.140891>.
- Lukaszewicz M, Simms N, Dudziak T, Nicholls J. Effect of steam flow rate and sample orientation on steam oxidation of ferritic and austenitic steels at 650 and 700°C. *Oxid Met.* 2013;79(5–6):473–548. <https://doi.org/10.1007/s11085-013-9358-2>.
- Dudziak T, Deodshumukh V, Backert L, Sobczak N, Witkowska M, Ratuszek W, Chruściel K, Zielinski A, Sobczak J, Bruzda G. Phase investigations under steam oxidation process at 800°C for 1000 h of advanced steels and Ni-based alloys. *Oxid Met.* 2017;87:139–58. <https://doi.org/10.1007/s11085-016-9662-8>.
- Dudziak T, Gajewski P, Śnieżyński B, Deodshumukh V, Witkowska M, Ratuszek W, Chruściel K. Neural network modeling studies of steam oxidised kinetic behaviour of advanced steels and ni-based alloys at 800°C for 3000 hours. *Corr Sci.* 2018;133(1):94–111. <https://doi.org/10.1016/j.corsci.2018.01.013>.
- Cao K, Yang W, Zhang J, Liu C, Qu P, Su H, Zhang J, Liu L. Solidification characteristics and as-cast microstructure of a Ru-containing nickel-based single crystal superalloy. *J Mater Res Technol.* 2021;11:474–86. <https://doi.org/10.1016/j.jmrt.2021.01.043>.
- Wyckoff R. Crystal structures. New York: Interscience; 1963.
- McClune F. New X-ray powder diffraction patterns from the JCPDS associateship. *Powder Diffract.* 1986;1:77–99.
- Bowman A, Arnold G, Storms E, Nereson N. The crystal structure of Cr₂₃C₆. *Acta Crystall B.* 1972;28:3102–3. <https://doi.org/10.1107/S0567740872007526>.
- Sims C, Stoloff N, Hagel W. Superalloys II. New York: Wiley-Interscience; 1987.
- Matysiak H, Zagorska M, Balkowiec A, Adamczyk-Cieslak B, Dobkowski K, Koralnik M, Cygan R, Nawrocki J, Cwajna J,

- Kurzydowski K. The influence of the melt-pouring temperature and inoculant content on the macro and microstructure of the IN713C Ni-based superalloy. *JOM*. 2016;68(1):185–97. <https://doi.org/10.1007/s11837-015-1672-5>.
32. Aigner K, Lengauer W, Rafaja D, Eittemayer P. Lattice parameters and thermal expansion of $Ti(C_xN_{1-x})$, $Zr(C_xN_{1-x})$, $Hf(C_xN_{1-x})$ and TiN_{1-x} from 298 to 1473 K as investigated by high-temperature X-ray diffraction. *J Alloys Compd*. 1994;215:121–6. [https://doi.org/10.1016/0925-8388\(94\)90828-1](https://doi.org/10.1016/0925-8388(94)90828-1).
 33. Momma K, Izumi F. VESTA 3 for three-dimensional visualization of crystal, volumetric and morphology data. *J Appl Crystall*. 2011;44:1272–6. <https://doi.org/10.1107/S002188911038970>.
 34. Guyard C, Barbangelo A, Allibert C, Driole J. Solidification path and phase equilibria in the liquid-solid range of cobalt-base alloy. *J Mater Sci*. 1981;16:604–12. <https://doi.org/10.1007/BF02402776>.
 35. Hamar-Thibault S, Durrand-Charre M, Andries B. Carbide transformation during aging of wear-resistant cobalt alloys. *Metall Mater Trans A*. 1982;13:545–50. <https://doi.org/10.1007/BF02644417>.
 36. Johansson T, Uhrenius B. Phase equilibria, isothermal reactions, and a thermodynamic study in the Co–W–C system at 1150°C. *Met Sci*. 1978;12(2):83–94. <https://doi.org/10.1179/msc.1978.12.2.83>.
 37. Jiang W, Yao X, Guan H, Hu Z. Secondary carbide precipitation in a directionally solidified cobalt-base superalloy. *Metall Mater Trans A*. 1999;30A:513–20. <https://doi.org/10.1007/s11661-999-0043-7>.
 38. Xie S, Wang T, Lu J, Yang H, Zhao G. Effects of Zr on microstructure and short-term strength in GH586. *J Mater Sci Technol*. 1999;15(5):415–8.
 39. Wallace W, Holt R, Terada T. The nature of the sulfo-carbides observed in nickel-base superalloys. *Metallography*. 1973;6:511–26. [https://doi.org/10.1016/0026-0800\(73\)90048-7](https://doi.org/10.1016/0026-0800(73)90048-7).
 40. Kudielka H, Rohde H. Structural investigation of the carbosulfides of titanium and zirconium. *Zeitschrift für Kristallographie (Crystalline Materials)*. 1960;114:441–56.
 41. Lobl K, Tuma G. Carbide precipitation and carbide equilibrium in the Co–Cr–C system. *Metal Sci Heat Treat*. 1973;15:21–3. <https://doi.org/10.1007/BF00648453>.
 42. Fedoseeva A, Tkachev E, Dudko V, Dudova N, Kaibyshev R. Effect of alloying on interfacial energy of precipitation/matrix in high-chromium martensitic steels. *J Mater Sci*. 2017;52:4197–209. <https://doi.org/10.1007/s10853-016-0654-5>.
 43. Skupień P, Radwański K, Gazdowicz J, Arabasz S, Wiedermann J, Szala J. Microstructure of MAR M509 cobalt-based superalloy in as-cast conditions and after heat treatment. *PIMŻ*. 2010;62(1):259–64 (in polish).
 44. Sklenička V, Kvapilová M, Král P, Dvořák J, Svoboda M, Podhorná B, Zýka J, Hrbáček K, Joch A. Degradation processes in high-temperature creep of cast cobalt-based superalloys. *Mater Charact*. 2018;144:479–89. <https://doi.org/10.1016/j.matchar.2018.08.006>.
 45. Wagner H, Hall A. The physical metallurgy of cobalt-base superalloys. Defense metals information center. Columbus: Battelle Memorial Institute; 1962.
 46. Cacciamani G, Roncallo G, Wang Y, Vacchieri E, Costa A. Thermodynamic modelling of a six component (C–Co–Cr–Ni–Ta–W) system for the simulation of cobalt based alloys. *J Alloys Compd*. 2018;730:291–310. <https://doi.org/10.1016/j.jallcom.2017.09.327>.
 47. Gui W, Zhang X, Zhang H, Sun X, Zheng Q. Melting of primary carbides in a cobalt-base superalloy. *J Alloys Compd*. 2019;787(30):152–7. <https://doi.org/10.1016/j.jallcom.2019.02.041>.
 48. Gui W, Zhang H, Yang M, Jin T, Sun X, Zheng Q. The investigation of carbides evolution in a cobalt-base superalloy at elevated temperature. *J Alloys Compd*. 2017;695(25):1271–8. <https://doi.org/10.1016/j.jallcom.2016.10.256>.
 49. Gui W, Zhang H, Yang M, Jin T, Sun X, Zheng Q. Influence of type and morphology of carbides on stress-rupture behavior of a cast cobalt-base superalloy. *J Alloys Compd*. 2017;728(25):145–51. <https://doi.org/10.1016/j.jallcom.2017.08.287>.
 50. Wielgosz E, Kargul T. Differential scanning calorimetry study of peritectic steel grades. *J Therm Anal Calorim*. 2015;119:1547–53. <https://doi.org/10.1007/s10973-014-4302-5>.
 51. Archana M, Jagadeeswara Rao C, Ningshen S, Philip J. High-temperature air and steam oxidation and oxide layer characteristics of alloy 617. *J Mater Eng Perform*. 2021;30:931–43. <https://doi.org/10.1007/s11665-020-05367-8>.
 52. Dooley R. Program on technology innovation: oxide growth and exfoliation on alloys exposed to steam. California: Energy Power Research Institute EPRI; 2007.
 53. Buscail H, Rolland R, Riffard F, Issartel C, Perrier S. Cobalt based alloy oxidation at high temperatures. *HAL*. 2017: 1–10. <https://hal.archives-ouvertes.fr/hal-01628823>
 54. Yeh A, Wang S, Cheng C, Chang Y, Chang S. Oxidation behaviour of Si-bearing Co-based alloys. *Oxid Met*. 2016;86:99–112. <https://doi.org/10.1007/s11085-016-9623-2>.

Publisher's Note Springer Nature remains neutral with regard to jurisdictional claims in published maps and institutional affiliations.

Springer Nature or its licensor holds exclusive rights to this article under a publishing agreement with the author(s) or other rightsholder(s); author self-archiving of the accepted manuscript version of this article is solely governed by the terms of such publishing agreement and applicable law.